Nanoscale

Check for updates

Three-dimensional carbon network confined antimony nanoparticle anodes for high-capacity K-ion batteries†

Chunhua Han, Kang Han, Xuanpeng Wang, Chenyang Wang, Qi Li, Jiashen Meng, Xiaoming Xu, Qiu He, Wen Luo, Liming Wu and Liqiang Mai [ID] *

Antimony (Sb) represents a promising anode for K-ion batteries (KIBs) due to its high theoretical capacity and suitable working voltage. However, the large volume change that occurs in the potassiation/depotassiation process can lead to severe capacity fading. Herein, we report a high-capacity anode material by *in situ* confining Sb nanoparticles in a three-dimensional carbon framework (3D SbNPs@C) *via* a template-assisted freeze-drying treatment and subsequent carbothermic reduction. The as-prepared 3D SbNPs@C hybrid material delivers high reversible capacity and good cycling stability when used as the anode for KIBs. Furthermore, cyclic voltammetry and *in situ* X-ray diffraction analysis were performed to reveal the intrinsic mechanism of a K–Sb alloying reaction. Therefore, this work is of great importance to understand the electrochemical process of the Sb-based alloying reaction and will pave the way for the exploration of high performance KIB anode materials.

1. Introduction

Owing to the continuous exhaustion of traditional fossil sources and aggravation of global environmental problems, exploiting sustainable and clean energy sources has attracted increasing attention.[1–4] Secondary batteries, benefiting from their high energy conversion efficiency and portability, have become one of the most promising devices to store energy.[5–8] With similar chemical properties, abundant natural resources and low cost of Na and K, great interest in Na-ion batteries (NIBs) and K-ion batteries (KIBs) has emerged.[9–13] Due to the standard hydrogen potential of K (-2.93 V *vs.* $E°$) being lower than that of Na (-2.71 V *vs.* $E°$) and closer to that of Li (-3.04 V *vs.* $E°$), making potassium can offer a lower reduction potential compared to making sodium. Therefore, PIBs have

more potential as low-cost batteries with high energy density and high voltage.[14,15] Over the past two years, considerable research efforts have been devoted to exploring optional materials for KIBs.[16–22] For anodes, recent advanced research on KIBs mainly focuses on carbon-based materials due to their high electric conductivity and low-cost.[23–26] Nevertheless, the capacities of carbonaceous materials are not satisfactory (<280 mA h g^{-1}) and cannot meet the ever-growing demand,[27] which seriously hinder their practical application. Especially, the large radius of K^+ ($Li^+ < Na^+ < K^+$, 0.76 Å < 1.02 Å < 1.38 Å) makes it extremely difficult to find a suitable electrode material that can accommodate the repeated K-ion insertion–extraction to achieve a stable cycling performance.[28–30] Therefore, developing a high-capacity anode is the hotspot and frontier of current studies on KIBs.

Recently, alloy-type electrodes have attracted considerable interest due to their appropriate potential and high theoretical specific capacities.[14,31–33] Among various alloy-based materials, antimony (Sb) is a promising anode material for KIBs with a high theoretical capacity of 660 mA h g^{-1}. However, the large volumetric change (~300%) during the potassiation/depotassiation processes may cause fracture of the active material and loss of electrical contact, resulting in rapid capacity fading.[34–37] To address this issue, numerous strategies have been proposed to relieve volume expansion and enhance the electrochemical performance of Sb-based anode materials.[38–41] One efficient and simple strategy is to tune the morphology and structure at the nanoscale. For instance, Liu *et al.*[42] constructed a unique Sb@C coaxial nanotube structure in which the outer nanotube provides enough space to accommodate the large volume expansion of Sb, showing much improved rate capability and cycling stability. Another feasible approach is to use carbonaceous materials as the buffer layer. In these materials, three-dimensional nanoarchitectures, such as 3D carbon network,[43] 3D graphene foam,[44] 3D graphene aerogel,[45] are generally considered to be an effective solution to maintain structural stability and ease volume expansion due to their high surface area, honeycomb-like interconnected networks and superior interfaces. Recently, Luo *et al.*[46] syn-

State Key Laboratory of Advanced Technology for Materials Synthesis and Processing, Wuhan University of Technology, Wuhan 430070, China.
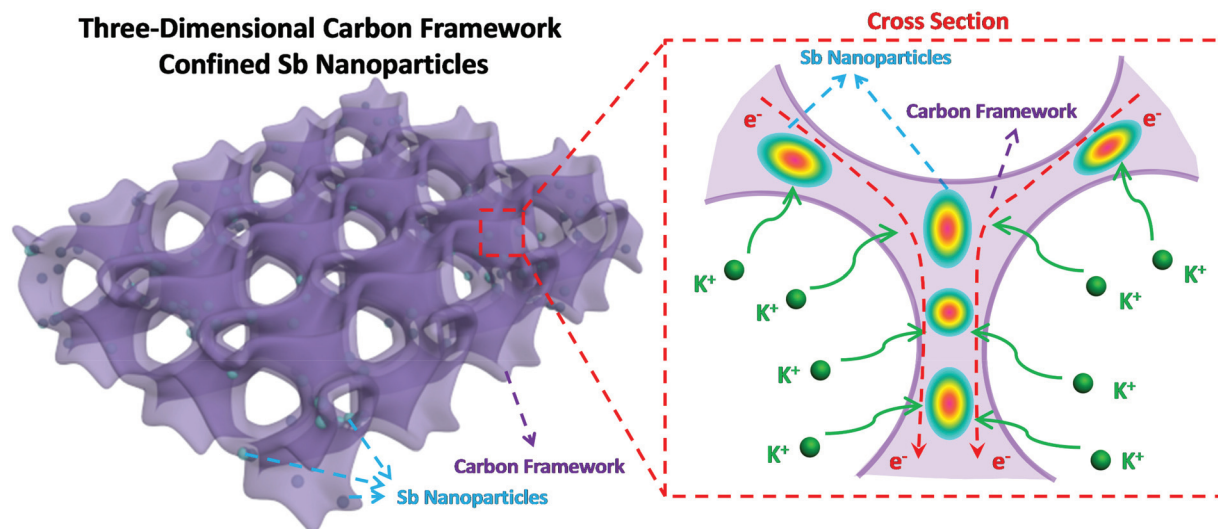*E-mail: mlq518@whut.edu.cn*

Fig. 1 Schematic illustration of the 3D SbNPs@C hybrid electrode with large electrode−electrolyte contact area, short K-ion diffusion distances and fast electron transport network.

thesized antimony with a three-dimensional carbon hybrid electrode for high-performance sodium energy storage, achieving stable cycling performance as well as superior rate capability.

Herein, we design and construct Sb nanoparticles confined in a honeycomb-like 3D carbon framework (denoted as 3D SbNPs@C) for high-performance potassium storage for the first time. As shown in Fig. 1, this structural design combines the merits of the 3D structure and the high capacity of the Sb anode. On one hand, the 3D structure network can not only act as a buffer layer to alleviate structural degradation, but also increase the effective contact area between electrode and electrolyte. On the other hand, the presence of a carbon matrix effectively limits the agglomeration of antimony particles and greatly enhances the conductivity of the electrode material. We believe that this work can bring some new ideas to exploit the alloy-based anode with high reversible capacity for KIBs.

2. Experimental

All the chemical reagents were purchased from commercial sources and used without further purification.

2.1. Synthesis of 3D SbNPs@C

The specific synthetic procedures for 3D SbNPs@C are as follows: first, 0.25 g polyvinyl pyrrolidone (PVP-K30) (Sigma-Aldrich, 99.99%) and 1.25 g citric acid (AR, 99%) were dissolved in deionized water (35 mL) to obtain a homogeneous solution. Then, $SbCl_3$ (0.456 g) (Macklin, 99.9%) and 10 g NaCl (AR, 99%) were added into the above solution, respectively. Stirring for 30 min, the as-obtained transparent solution was rapidly frozen in liquid nitrogen. Subsequently, the water in the mixture was removed by freeze-drying and the obtained sponge-like sample was ground into a fine powder, and then

subjected to heat treatment. Specifically, the composite powder was placed in a quartz boat located in a tube furnace and heated at 700 °C for 6 h at a heating rate of 2 °C min^{-1} under H_2/Ar (v/v = 5/95). Finally, the as-synthesized products were washed with deionized water several times to remove the NaCl template, and 3D SbNPs@C was obtained.[39,41]

2.2 Synthesis of three-dimensional carbon (3D-C)

The synthesis method of 3D-C is similar to that of 3D SbNPs@C in the preparation process. The only difference is that $SbCl_3$ is not added to the solution during the synthesis of 3D-C.

2.3. Materials characterization

The morphologies of the samples were investigated by field-emission scanning electron microscopy (FESEM; JEOL JSM-7100FA) and transmission electron microscopy (TEM, JEM-2100F, 200 kV). Energy dispersive spectra (EDS) were used for elemental analysis. The XRD patterns were collected by powder X-ray diffraction using a D8 Discover X-ray diffractometer, with Cu Kα radiation (λ = 1.5418 Å). Thermogravimetric analysis (TGA) was performed using a Netzsch STA 449C simultaneous analyzer and the sample was heated from room temperature to 800 °C in air at a heating rate of 10 °C min^{-1}. Raman spectra experiments were carried out with He–Ne laser excitation at 633 nm using a Horiba Jobin Yvon Lab RAM HR800 Raman spectrometer.

In situ XRD experiment during the electrochemical testing of the battery was performed on a Bruker D8 Discover X-ray diffractometer with a non-monochromated Cu Kα X-ray source scanned at the 2θ range of 19–40°. For *in situ* XRD measurement, the electrode was placed right behind an X-ray-transparent beryllium window which also acted as a current collector. The *in situ* XRD signals were collected using a planar detector

in still mode during the charge/discharge processes, and each pattern took 120 s to acquire.

2.4. Electrochemical measurements

The electrochemical measurements were carried out by using 2016 coin cells, which were assembled in a glove box filled with pure argon gas, and used K metal (99.5%, Sigma-Aldrich) as the reference electrode. The electrolyte was composed of 0.8 M KPF_6 dissolved in EC/DEC (ethylene carbonate/diethyl carbonate) with a volume ratio of 1 : 1 and a Whatman glass microfiber filter (Grade GF/F) as the separator.

The working electrodes were prepared by mixing the as-synthesized materials (3D SbNPs@C), acetylene black, and Carboxylmethyl Cellulose (CMC) at the weight ratio of 7 : 2 : 1. The slurry was cast onto Cu foil and dried in a vacuum oven at 70 °C overnight. The anodes were cut into square slices with ~0.49 cm^2 area and ~0.1 mm thickness and the average electrode mass loading obtained was about 1.4–1.8 mg cm^{-2}. The cells were aged for 6 h before the charge/discharge process to ensure full filtration of the electrolyte into the electrodes.

The capacity was calculated based on the total mass of the composite. The electrochemical performance of the cells was tested using a Land Battery Test System with a cut-off voltage range from 0.01 to 2.0 V (vs. K$^+$/K). Cyclic voltammetry and impedance testing were performed using a Biologic VMP-3 electrochemical workstation from 0.01 to 2.0 V at a scan rate of 0.1 mV s^{-1}.

3. Results and discussion

3.1. Morphology and structural characterization

The X-ray diffraction (XRD) pattern of the as-prepared 3D SbNPs@C samples is highly consistent with that of commercial Sb and can be well indexed to the rhombohedral phase of Sb (JCPDS No. 085-1323), manifesting that Sb^{3+} was completely reduced to metallic Sb after thermal reduction (Fig. 2a).[28,33,35] Scanning electron microscopy (SEM) images show that the obtained 3D SbNPs@C have a well-interconnected framework and numerous antimony nanoparticles are anchored in the 3D
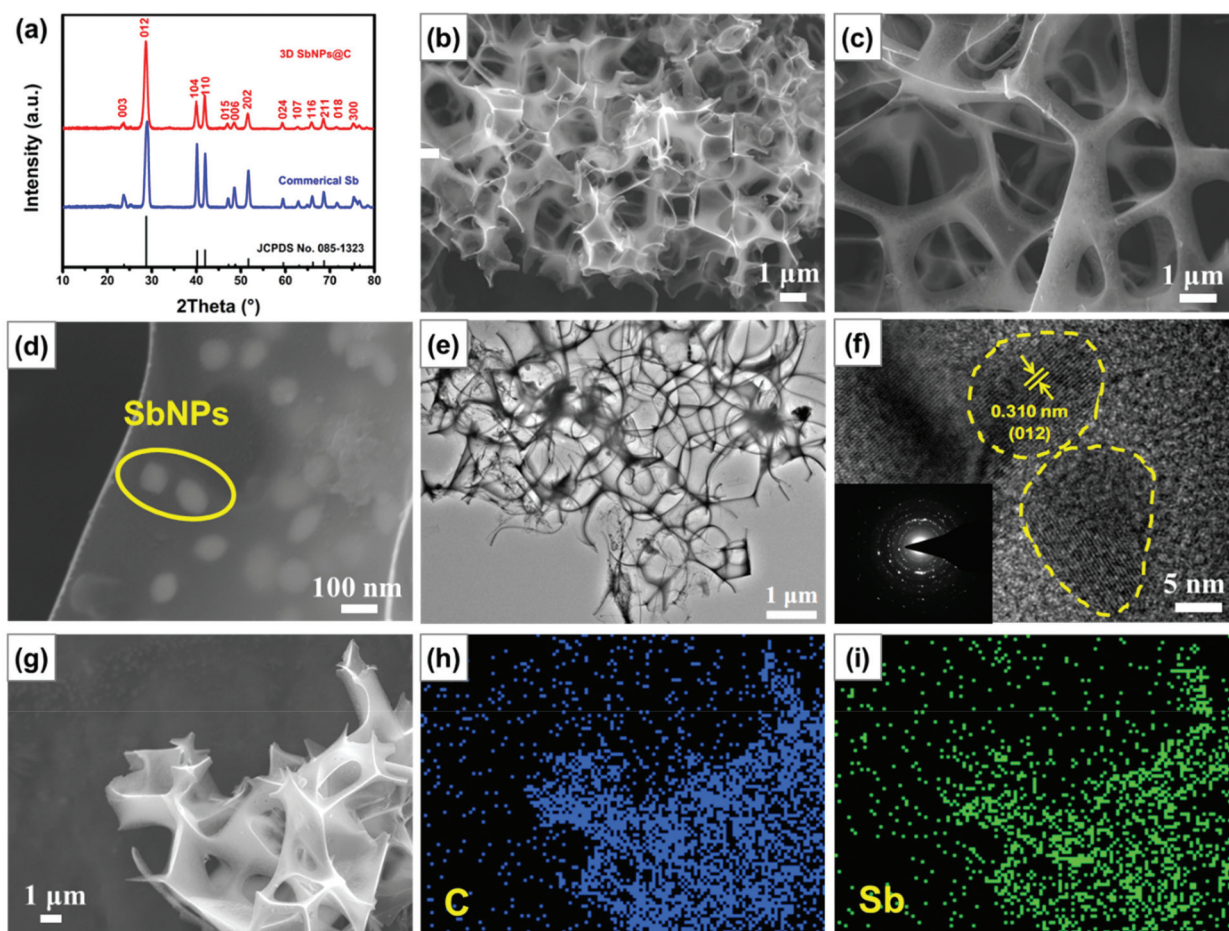
Fig. 2 Structure and morphology characterization of the 3D SbNPs@C composite. (a) XRD patterns of 3D SbNPs@C and commercial Sb, respectively. (b–d) SEM images of the 3D SbNPs@C composite at different magnifications. (e and f) TEM and HRTEM images of 3D SbNPs@C. (g–i) The EDS mapping images of 3D SbNPs@C.

carbon network, forming a honeycomb-like structure (Fig. 2b and c).

Compared with bulk commercial Sb, this unique structure can effectively shorten the ion diffusion distance and endow the entire electrode with outstanding electron transport properties (Fig. S1†).[47] Moreover, as shown in Fig. 2d, the sizes of the individual antimony particles are in the range of 60–100 nm. TEM images of 3D SbNPs@C also display a clear 3D honeycomb-like structure and many tiny antimony particles embedded in the 3D carbon network (Fig. 2e), which is highly in accordance with the morphology characterization observed by SEM. High-resolution transmission electron microscopy (HRTEM) was used to further explore the microstructure of 3D SbNPs@C. As shown in Fig. 2f, the obtained sample shows the characteristic spacing of 0.31 nm, corresponding to the (012) lattice planes of metallic Sb. The elemental mapping results (Fig. 2g–i) further confirm the presence of Sb and C, and verify that these two components are uniformly distributed in 3D SbNPs@C. Such a unique structure of confined SbNPs in the 3D carbon network is expected to suppress the agglomeration of SbNPs and improve the electrical conductivity of the electrode to achieve a high-capacity anode.

Raman spectroscopy was also implemented to evaluate the composition of 3D SbNPs@C. As shown in Fig. S2,† one weak Raman peak located at 143 cm^{-1}, corresponding to the characteristic signal of Sb, was observed.[35,39] Compared with the pure commercial Sb powder, the Raman shifts located at ~1354 and ~1585 cm^{-1} can be attributed to the D- and G-bands of carbon materials, respectively. The ratio of D-band and G-band (I_D/I_G) in 3D SbNPs@C is calculated to be about

0.95, suggesting the presence of a high degree of disorder and large defects in the 3D SbNPs@C structure.[48] The mass content of Sb in 3D SbNPs@C was also investigated by thermogravimetric analysis (TGA). The slight weight gain that occurred at 300 °C–430 °C can be attributed to the formation of the final oxidation product Sb$_2$O$_3$, and the dramatic weight loss between 430 °C and 500 °C can be ascribed to the combustion of carbon (Fig. S3†).[42] Therefore, the Sb content in the hybrid composite is calculated to be 61 wt%. The N$_2$ adsorption/desorption isotherm of 3D SbNPs@C displays a type IV isotherm with a distinct hysteresis loop at the relative pressure P/P_0 ranging from 0.5 to 1 (Fig. S4†), suggesting the existence of both micropores and mesopores, which are consistent with the Barrett–Joyner–Halenda (BJH) pore-size peaks centered at 4.1 nm. Meanwhile, the 3D SbNPs@C sample possesses a surface area of 38 m^2 g^{-1} based on the Brunauer–Emmett–Teller (BET) result.

3.2 Electrochemical performance

The electrochemical performance of the 3D SbNPs@C composite as a KIB anode was investigated in a voltage window of 0.01–2.0 V (vs. K$^+$/K). Fig. 3a shows the typical cyclic voltammograms (CVs) of the 3D SbNPs@C electrode for the first three cycles at a scan rate of 0.1 mV s^{-1}. It clearly shows two potassiation peaks and two depotassiation peaks, suggesting that the alloying is a two-step process and may generate an intermediate K–Sb phase during the potassiation/depotassiation process.[49] The first cathodic scan is slightly different from the subsequent scans, indicating an activation process occurring in the first cycle.[35,50] More specifically, the alloying peaks at
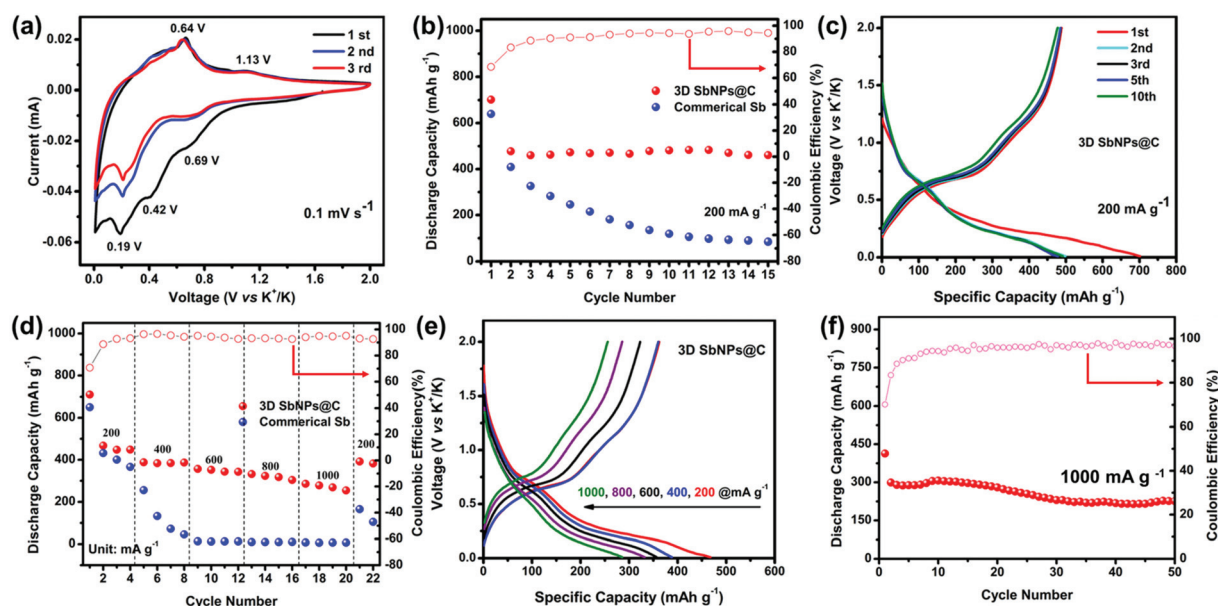
Fig. 3 Electrochemical performance of the 3D SbNPs@C electrode. (a) CV curves of 3D SbNPs@C between 0.01 and 2 V at a scan rate of 0.1 mV s^{-1}. (b) Cycling performance of 3D SbNPs@C and commercial Sb electrode at a specific current density of 200 mA g^{-1}. (c) Representative charge–discharge curves of the 3D SbNPs@C electrode at a specific current density of 200 mA g^{-1}. (d) Rate performance of 3D SbNPs@C and commercial Sb. (e) Charge and discharge curves of the 3D SbNPs@C electrode at different current densities. (f) Cycling performance of the 3D SbNPs@C electrode at a specific current density of 1000 mA g^{-1} and the corresponding coulombic efficiency.

0.69 and 0.19 V may be ascribed to the electrochemical reaction of Sb to form amorphous K_xSb and then cubic K_3Sb, respectively. Similarly, the dealloying peaks at 0.64 V and 1.13 V may be related to the electrochemical oxidation of cubic K_3Sb to form amorphous K_xSb and then amorphous Sb.[42] In addition, a lower cathodic peak is detected at 0.42 V in the first potential sweep process, corresponding to the formation of a solid electrolyte interface (SEI) between electrodes and electrolyte.[39] From the second potential sweep onward, two pairs of potassiation–depotassiation peaks at 0.19/0.69 V and 0.64/1.13 V are well-overlapped, exhibiting good stability and reversibility of the 3D SbNPs@C anode.

Fig. 3b compares the cycling performance of 3D SbNPs@C and commercial Sb electrode at the current density of 200 mA g^{-1}; the 3D SbNPs@C electrode achieves 701 mA h g^{-1} in the first cycle and maintains 488 mA h g^{-1} in the second cycle, retaining 461 mA h g^{-1} after 15 cycles (the capacity retention rate is 96%, relative to the second cycle). In contrast, the capacity of bulk commercial Sb displays a significant decrease in the cycling performance test and only retains 85 mA h g^{-1} after 15 cycles (the capacity retention rate is 21%, relative to the second cycle), demonstrating the great cycling performance of 3D SbNPs@C. The initial coulombic efficiency (CE) of the 3D SbNPs@C electrode is about 70%. The large irreversible capacities are attributed to the formation of the solid–electrolyte interface (SEI) layer. During the subsequent cycles, the CE gradually increased and eventually stabilized at about 98%, suggesting a high electrochemical reversibility for KIBs. In addition, given the low mass content of carbon in the hybrid electrode (~39 wt%) and the low intrinsic capacity of 3D-C (~120 mA h g^{-1}, Fig. S5†), the capacity contribution from 3D-C in the 3D SbNPs@C hybrid anode is about 47 mA h g^{-1}.

The superiority of 3D SbNPs@C compared to commercial Sb is revealed by further electrochemical analyses. Representative charge–discharge galvanostatic cycling profiles at a current density of 200 mA g^{-1} are presented in Fig. 3c and Fig. S6.† During the first discharge process, both samples show a smooth slope below 0.5 V and a long plateau at around 0.2 V. In the second and the following discharge profiles, only one plateau was observed in the commercial Sb anode, suggesting the disintegration of the bulk Sb anode. However, the 3D SbNPs@C electrode still displays two obvious plateaus around 0.69 V and 0.19 V, which correspond to the two-step alloying reaction and are highly consistent with the CV curves of Fig. 3a. The highly overlapped charge–discharge profiles demonstrate that these unique SbNPs anchored in the 3D carbon framework structure have good structural stability.

The rate performance of the 3D SbNPs@C and commercial Sb electrodes is presented in Fig. 3d, where the current density increased step-wise from 200 to 1000 mA g^{-1} and returned to 200 mA g^{-1}. As shown, 3D SbNPs@C consistently outperforms its commercial Sb counterpart. The average specific capacities for 3D SbNPs@C are 478, 390, 361, 334 and 288 mA h g^{-1} at the current densities of 200, 400, 600, 800 and 1000 mA g^{-1}, respectively (Fig. S7†). When the current density returned to 200 mA g^{-1}, the 3D SbNPs@C electrode still retains a revers-

ible capacity of 392 mA h g^{-1}, suggesting good rate performance and cycling stability. Fig. 3e shows that both discharge and charge profiles have good reproducibility at different current densities.

To prove the structural stability of the unique 3D SbNPs@C anode material, long-term cycling stability of 3D SbNPs@C at a high current density of 1000 mA g^{-1} over 50 cycles is presented (Fig. 3f). A reversible capacity of 225 mA h g^{-1} is achieved over a long-time charge/discharge process with a capacity fading of only 0.4% per cycle. Besides, the structural stability of the 3D structure was investigated by disassembling the coin cell after 10, 30, and 50 cycles, respectively. SEM analyses (Fig. S8†) revealed that no significant structural changes were observed between the pristine and cycled 3D SbNPs@C anode. The electrochemical impedance spectroscopy (EIS) plots (Fig. S9†) reveal that the charge-transfer resistance of 3D SbNPs@C is smaller than those of commercial Sb. The enhancement is attributed to the interfacial effect of 3D SbNPs@C, which provides an orientated electronic transport pathway, giving it high ion-diffusion coefficient and facilitating interfacial electron transport.[36,44] To the best of our knowledge, 3D SbNPs@C as an anode material for KIBs exhibits superior electrochemical performance compared with other related reports in terms of discharge capacity and rate performance (Table S1†).

3.3. Potassium storage mechanism

To investigate the alloying mechanism of 3D SbNPs@C in KIBs, *in situ* XRD experiments were performed for the first two cycles. As seen in Fig. 4, only a well-defined peak of crystalline Sb located at 28.6°, corresponding to the (012) face of Sb, is detectable in the diffraction pattern at the beginning of the reaction. During the first discharge process, the main (012) peak becomes weaker and gradually disappears. Nevertheless,
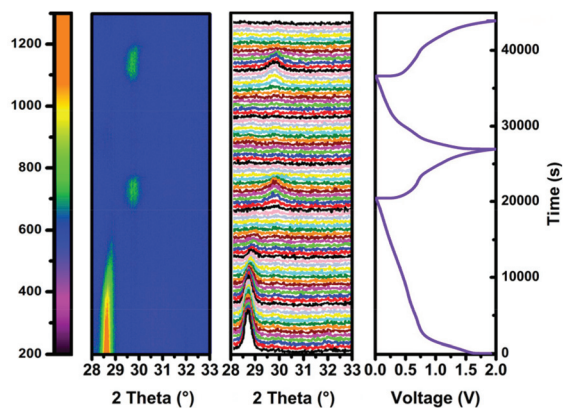

Fig. 4 *In situ* XRD patterns of the 3D SbNPs@C electrode during the galvanostatic depotassiation/potassiation process at 100 mA g^{-1}. The image plot of the diffraction patterns at 28–33° during the first two cycles. The horizontal axis represents the selected 2θ regions, and time is on the vertical axis. The diffraction intensity is color coded with the scale bar shown on left. The corresponding diffraction intensity is color coded with the scale bar shown on left.

when discharged to 0.19 V, a new diffraction peak appears at 29.7°, which can be well indexed to K_3Sb (JCPDS No. 89-4001) (Fig. S10†). The fact that K_3Sb only appears after the vanishing of the diffraction peak of Sb implies the formation of an amorphous intermediate phase in this process.[51] On the basis of this discussion, a two-step potassiation process was presented. First, the crystalline Sb breaks down and is gradually transformed into an intermediate amorphous phase K_xSb ($0 < x < 3$), and finally, crystallizes to cubic K_3Sb. Upon charging, the signals of K_3Sb gradually decrease accompanied by the emergence of the intermediate phase of K_xSb. With further charging, the intermediate phase of K_xSb gradually transformed into amorphous Sb, which is similar to the case in sodium ion batteries.[49,51,52] Meanwhile, *ex situ* TEM results (Fig. S11†) further verify that the product is amorphous Sb at the end of charging. In brief, the alloying mechanism of the 3D SbNPs@C electrode can be summarized as the following reactions:

$$Sb + x\,K^+ + x\,e^- \leftrightarrow K_xSb \quad (1)$$

$$K_xSb + (3-x)\,K^+ + 3 - x\,e^- \leftrightarrow K_3Sb \quad (2)$$
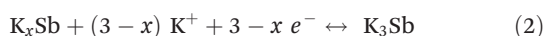
4. Conclusions

In summary, the 3D SbNPs@C hybrid electrode, synthesized by a simple freeze-drying method followed by conventional carbothermic reduction, was used as an anode in KIBs for the first time. The strong confinement of SbNPs to the 3D carbon network is the key for achieving a stable electrode architecture to endure repeatable potassiation/depotassiation cycles. In addition, the 3D conductive carbon framework enhances the electrical conductivity of the electrode and serves as a buffer matrix to accommodate the volume changes, maintaining the integrity of the electrode. Compared with commercial Sb, the 3D SbNPs@C electrode delivers a high reversible capacity ($\sim$478 mA h g^{-1} at 200 mA g^{-1}) and superior rate capability ($\sim$288 mA h g^{-1} at 1000 mA g^{-1}). Moreover, our investigation of the reaction mechanisms of 3D SbNPs@C in KIBs indicates that the alloying is a two-step process in which an intermediate phase K_xSb and the K_3Sb phase are formed during the potassiation–depotassiation process. We believe that this work could potentially promote further study on alloy-based anode materials and pave the way for the development of high performance of KIBs.

Author contributions

Liqiang Mai and Kang Han contributed the central idea, Kang Han and Chunhua Han analysed most of the data, and wrote the initial draft of the paper. The remaining authors contributed to refining the ideas, carrying out additional analyses and finalizing this paper. All authors discussed the results and revised the manuscript.

Conflicts of interest

There are no conflicts to declare.

Acknowledgements

Notes and references

1 S. Liu, J. Feng, X. Bian, J. Liu, H. Xu and Y. An, *Energy Environ. Sci.*, 2017, **10**, 1222–1233.

2 J. Peters, D. Buchholz, S. Passerini and M. Weil, *Energy Environ. Sci.*, 2016, **9**, 1744–1751.

3 C. L. Zhang, Y. Xu, M. Zhou, L. Y. Liang, H. S. Dong, M. H. Wu, Y. Yang and Y. Lei, *Adv. Funct. Mater.*, 2017, **27**, 1604307.

4 X. Wang, P. Hu, C. Niu, J. Meng, X. Xu, X. Wei, C. Tang, W. Luo, L. Zhou, Q. An and L. Mai, *Nano Energy*, 2017, **35**, 71–78.

5 L. Mai, Q. Wei, Q. An, X. Tian, Y. Zhao, X. Xu, L. Xu, L. Chang and Q. Zhang, *Adv. Mater.*, 2013, **25**, 2969–2973.

6 H. L. Pan, Y. S. Hu and L. Q. Chen, *Energy Environ. Sci.*, 2013, **6**, 2338–2360.

7 S. Lu, Y. Cheng, X. Wu and J. Liu, *Nano Lett.*, 2013, **13**, 2485–2489.

8 Y. Hou, Y. Cheng, T. Hobson and J. Liu, *Nano Lett.*, 2010, **10**, 2727–2733.

9 Y. Lu, N. Zhang, S. Jiang, Y. Zhang, M. Zhou, Z. Tao, L. A. Archer and J. Chen, *Nano Lett.*, 2017, **17**, 3668–3674.

10 H. Y. Kang, Y. C. Liu, K. Z. Cao, Y. Zhao, L. F. Jiao, Y. J. Wang and H. T. Yuan, *J. Mater. Chem. A*, 2015, **3**, 17899–17913.

11 L. M. Wu, D. Buchholz, D. Bresser, L. G. Chagas and S. Passerini, *J. Power Sources*, 2014, **251**, 379–385.

12 L. Wu, D. Bresser, D. Buchholz, G. A. Giffin, C. R. Castro, A. Ochel and S. Passerini, *Adv. Energy Mater.*, 2015, **5**, 1401142.

13 D. P. Leonard, Z. Wei, G. Chen, F. Du and X. Ji, *ACS Energy Lett.*, 2018, **3**, 373–374.

14 W. Zhang, J. Mao, S. Li, Z. Chen and Z. Guo, *J. Am. Chem. Soc.*, 2017, **139**, 3316–3319.

15 X. Wu, D. P. Leonard and X. Ji, *Chem. Mater.*, 2017, **29**, 5031–5042.

16 S. K. Chong, Y. Z. Chen, Y. Zheng, Q. Tan, C. Y. Shu, Y. N. Liu and Z. P. Guo, *J. Mater. Chem. A*, 2017, **5**, 22465–22471.

17 Y. J. Liu, Z. X. Tai, Q. Zhang, H. Q. Wang, W. K. Pang, H. K. Liu, K. Konstantinov and Z. P. Guo, *Nano Energy*, 2017, **35**, 36–43.

18 X. Wang, X. Xu, C. Niu, J. Meng, M. Huang, X. Liu, Z. Liu and L. Mai, *Nano Lett.*, 2017, **17**, 544–550.

19 H. Gao, T. F. Zhou, Y. Zheng, Q. Zhang, Y. Q. Liu, J. Chen, H. K. Liu and Z. P. Guo, *Adv. Funct. Mater.*, 2017, **27**, 1702634.

20 V. Lakshmi, Y. Chen, A. A. Mikhaylov, A. G. Medvedev, I. Sultana, M. M. Rahman, O. Lev, P. V. Prikhodchenko and A. M. Glushenkov, *Chem. Commun.*, 2017, **53**, 8272–8275.

21 I. Sultana, T. Ramireddy, M. M. Rahman, Y. Chen and A. M. Glushenkov, *Chem. Commun.*, 2016, **52**, 9279–9282.

22 Z. Jian, Z. Xing, C. Bommier, Z. Li and X. Ji, *Adv. Energy Mater.*, 2016, **6**, 1501874.

23 L. Fan, Q. Liu, S. Chen, K. Lin, Z. Xu and B. Lu, *Small*, 2017, **13**, 1701011.

24 Z. L. Jian, S. Hwang, Z. F. Li, A. S. Hernandez, X. F. Wang, Z. Y. Xing, D. Su and X. L. Ji, *Adv. Funct. Mater.*, 2017, **27**, 1700324.

25 X. Wang, K. Han, D. Qin, Q. Li, C. Wang, C. Niu and L. Mai, *Nanoscale*, 2017, 18216–18222.

26 Z. Jian, W. Luo and X. Ji, *J. Am. Chem. Soc.*, 2015, **137**, 11566–11569.

27 J. C. Pramudita, D. Sehrawat, D. Goonetilleke and N. Sharma, *Adv. Energy Mater.*, 2017, **7**, 1602911.

28 W. D. McCulloch, X. Ren, M. Yu, Z. Huang and Y. Wu, *ACS Appl. Mater. Interfaces*, 2015, **7**, 26158–26166.

29 X. Y. Wu, D. P. Leonard and X. L. Ji, *Chem. Mater.*, 2017, **29**, 5031–5042.

30 A. Eftekhari, Z. Jian and X. Ji, *ACS Appl. Mater. Interfaces*, 2017, **9**, 4404–4419.

31 Y. An, H. Fei, Z. Zhang, L. Ci, S. Xiong and J. Feng, *Chem. Commun.*, 2017, **53**, 8360–8363.

32 G. Y. Ma, K. S. Huang, J. S. Ma, Z. C. Ju, Z. Xing and Q. C. Zhuang, *J. Mater. Chem. A*, 2017, **5**, 7854–7861.

33 I. Sultana, M. M. Rahman, Y. Chen and A. M. Glushenkov, *Adv. Funct. Mater.*, 2018, **28**, 1703857.

34 D. Bresser, S. Passerini and B. Scrosati, *Energy Environ. Sci.*, 2016, **9**, 3348–3367.

35 G. H. Wang, X. H. Xiong, Z. H. Lin, C. H. Yang, Z. Lin and M. L. Liu, *Electrochim. Acta*, 2017, **242**, 159–164.

36 L. Wu, X. Hu, J. Qian, F. Pei, F. Wu, R. Mao, X. Ai, H. Yang and Y. Cao, *Energy Environ. Sci.*, 2014, **7**, 323–328.

37 H. Xie, W. P. Kalisvaart, B. C. Olsen, E. J. Luber, D. Mitlin and J. M. Buriak, *J. Mater. Chem. A*, 2017, **5**, 9661–9670.

38 J. H. Song, P. F. Yan, L. L. Luo, X. G. Qi, X. H. Rong, J. M. Zheng, B. W. Xiao, S. Feng, C. M. Wang, Y. S. Hu, Y. H. Lin, V. L. Sprenkle and X. L. Li, *Nano Energy*, 2017, **40**, 504–511.

39 X. Xu, Z. F. Dou, E. L. Gu, L. Si, X. S. Zhou and J. C. Bao, *J. Mater. Chem. A*, 2017, **5**, 13411–13420.

40 Z. Yi, Q. G. Han, X. Li, Y. M. Wu, Y. Cheng and L. M. Wang, *Chem. Eng. J.*, 2017, **315**, 101–107.

41 Q. Q. Yang, J. Zhou, G. Q. Zhang, C. Guo, M. Li, Y. C. Zhu and Y. T. Qian, *J. Mater. Chem. A*, 2017, **5**, 12144–12148.

42 Z. M. Liu, X. Y. Yu, X. W. D. Lou and U. Paik, *Energy Environ. Sci.*, 2016, **9**, 2314–2318.

43 Z. Chen, W. Ren, L. Gao, B. Liu, S. Pei and H. M. Cheng, *Nat. Mater.*, 2011, **10**, 424–428.

44 H. Ji, L. Zhang, M. T. Pettes, H. Li, S. Chen, L. Shi, R. Piner and R. S. Ruoff, *Nano Lett.*, 2012, **12**, 2446–2451.

45 Y. Zhou, Q. Liu, D. Liu, H. Xie, G. Wu, W. Huang, Y. Tian, Q. He, A. Khalil, Y. A. Haleem, T. Xiang, W. Chu, C. Zou and L. Song, *Electrochim. Acta*, 2015, **174**, 8–14.

46 W. Luo, P. F. Zhang, X. P. Wang, Q. D. Li, Y. F. Dong, J. C. Hua, L. Zhou and L. Q. Mai, *J. Power Sources*, 2016, **304**, 340–345.

47 H. Sun, L. Mei, J. Liang, Z. Zhao, C. Lee, H. Fei, M. Ding, J. Lau, M. Li, C. Wang, X. Xu, G. Hao, B. Papandrea, I. Shakir, B. Dunn, Y. Huang and X. Duan, *Science*, 2017, **356**, 599–604.

48 T. Wu, H. Hou, C. Zhang, P. Ge, Z. Huang, M. Jing, X. Qiu and X. Ji, *ACS Appl. Mater. Interfaces*, 2017, **9**, 26118–26125.

49 P. K. Allan, J. M. Griffin, A. Darwiche, O. J. Borkiewicz, K. M. Wiaderek, K. W. Chapman, A. J. Morris, P. J. Chupas, L. Monconduit and C. P. Grey, *J. Am. Chem. Soc.*, 2016, **138**, 2352–2365.

50 X. H. Xiong, C. H. Yang, G. H. Wang, Y. W. Lin, X. Ou, J. H. Wang, B. T. Zhao, M. L. Liu, Z. Lin and K. Huang, *Energy Environ. Sci.*, 2017, **10**, 1757–1763.

51 A. Darwiche, C. Marino, M. T. Sougrati, B. Fraisse, L. Stievano and L. Monconduit, *J. Am. Chem. Soc.*, 2012, **134**, 20805–20811.

52 B. Kong, L. Zu, C. Peng, Y. Zhang, W. Zhang, J. Tang, C. Selomulya, L. Zhang, H. Chen, Y. Wang, Y. Liu, H. He, J. Wei, X. Lin, W. Luo, J. Yang, Z. Zhao, Y. Liu, J. Yang and D. Zhao, *J. Am. Chem. Soc.*, 2016, **138**, 16533–16541.